to give a rate of about 5% of the events taken with the second level triggers. The downscaling factors are software loadable and the typical values used in the 1990 run are listed in Table 4.1.

Table 4.1: List of parallel triggers with their downscaling factors.

Trigger Type	Downscaling factor
1p	16
1n	8
2p	3
2n	1
3p	1
3n	1
Pre-triggers	2001
Beam triggers	4001
MT triggers	22

2 Scalers

There are several types of scalers used in the experiment for various measurements. They are;

- *Spill Scalers* – Spill scalers keep track of the total number of beam particles, the number of gated beam particles (as defined by the beam telescope), and the number of events that are used in each trigger. They are read out and cleared at the end of each spill. These scalers are essential for cross section measurements.
- *Latching Scalers* – Latching scalers are used to measure the time at which each event occurred with respect to the previous beam particle, the beginning of the spill, the phase of 60Hz power lines, the previous clear etc. In addition, these are used to measure the instantaneous rate of the beam. These scalers are useful to study noise problems and other electronic problems.
- *Down Scalers* – The sole purpose of down scalers are to prescale different triggers so as to equalize their rates as described earlier. A section of these scalers are used to count the total number of triggers of a given type that is read out at the end of the spill.

3 Data Sample

The data selected through the online trigger requirements were written on 6250 BPI magnetic tapes. A data taking "run" consists of data taken until a tape is filled, which corresponds to approximately 8,000 to 9,000 complete, independent, event records. Each tape is labeled according to the order in which the data have been recorded.

The recorded peripheral data sample consists of two major parts, namely, a single nucleon emission (1p or 1n, designated as the 1p–1n sample) and two or three nucleon emissions (2p, 2n or higher, designated as 2p–2n sample). These were recorded over 6 different targets, and included the data taken with an empty target frame. In addition, a majority of the events were recorded with an online trigger requirement to enrich the data sample. To study trigger efficiencies, a small percentage of the data were taken without the online veto requirement. The recorded data sample is shown in Table 4.2.

Table 4.2: List of magnetic tapes written for each target and each trigger type.

Target	1p–1n	2p–2n or rare	Pre-trigger	Beam trigger	Pulser
Pb	8	36	6	6	6
Sn	7	36	3	3	3
Cu	3	37	3	3	3
Al	5	35	3	3	4
C	3	–	–	–	–
MT	4	33	3	3	3

The original data written in 6250 tapes were copied onto 8mm tapes which were read via exabyte tape drivers. Each 8mm tape is used to record up to 12 independent runs from 6250 tapes organized according to the target and trigger types. The peripheral data sample consists of 6 8mm tapes for 1p–1n triggers and 22 tapes for 2p–2n or rare trigger types. The total sample consists of about 2,400,000 events. These were fully analyzed in a Silicon Graphics computer (Personal Iris).

B Offline Selection

A large portion of the data written in the original 8mm tapes cannot be considered as good candidates for peripheral collisions, due to various factors such as interactions upstream and downstream of the target, problems in the detectors during the data taking run, etc. The offline analysis described in this section is mainly involved in reducing the data sample, by selecting good candidates for electromagnetic or soft nuclear fragmentation. The selected data were extracted and written into a secondary set of 8 mm tapes for further studies.

All detectors were calibrated and corrected for short term as well as long term gain variations prior to the offline selection procedure.

1 Good Beam Selection

1.1 Beam Scintillators

The trigger uses the beam scintillators to identify good beam particles. However, beam particles which interact with the materials upstream of the target, or two beam particles arriving within a very short time interval (double beams) could be recorded as good beam particles by slipping through the selections in the online trigger. Therefore additional offline selections were imposed on the measurements of the beam scintillators.

Figures 4.1 (a) and (b) show the histograms of the average pulse heights measured in counters S1 and S3. Each of these counters are read out by 4 phototubes connected through light guides placed symmetrically around the counters. Due to a noise problem in one of the signals, only 3 signals were used to perform the average for S3. The tail at low pulse height is a result of a pulse height measurement being distorted by a pileup effect in the phototubes. Figure 4.1 (c) is a two dimensional histogram which shows the time measured between the event under consideration and the previous event (time after the previous beam) versus the measured pulse height in S1. The data showing candidates at short times ($t<8$ μs) indicate the effect due to the pileup. These events are not produced by upstream interactions. The events with pulse heights greater than 100 in S1 and 75 in S3 were rejected.

Figure 4.1 (d) shows the average pulse height measured in the S2 and S4 counters. Each of these scintillators are connected to 2 phototubes mounted at opposite ends. In this scale the pulse height corresponding to the ^{28}Si beam is normalized to 100 counts. The measurement provides a resolution of 10% for Z=14 particles. The gain variations in the phototubes were corrected on a run by run basis. Events with counts less than 50 or greater than 150 were rejected.

1.2 Upstream Silicon Detector

The upstream silicon detector provides an additional pulse height measurement to select Z=14 beam particles. Since this detector is mounted just upstream of the target, it is able to detect the interactions in the beam scintillator system. However, this detector too suffers from serious pileup effects. Figure 4.2 (a) shows the measured time after previous beam against the measured pulse height for beam particles. We observe in Figure 2 that the pileup effect occurs when the beam particles arrive within a few μsecs of each other. This is due to the contribution of the negative going tail of the previous pulse on the present pulse, since the preamplifiers used in this detector have long shaping time. Events closer than 2.5 μsec were not used in this analysis.

Figure 4.2 (b) shows the measured pulse height in this detector after rejecting the events arriving less than 2.5 μsec from the previous beam particle. A resolution of 5% was obtained with this detector. The Z=14 particles were normalized to 1000 counts in this scale. Corrections were made for gain variations on a run by run basis. Events with counts less than 750 or greater than 1250 were rejected.

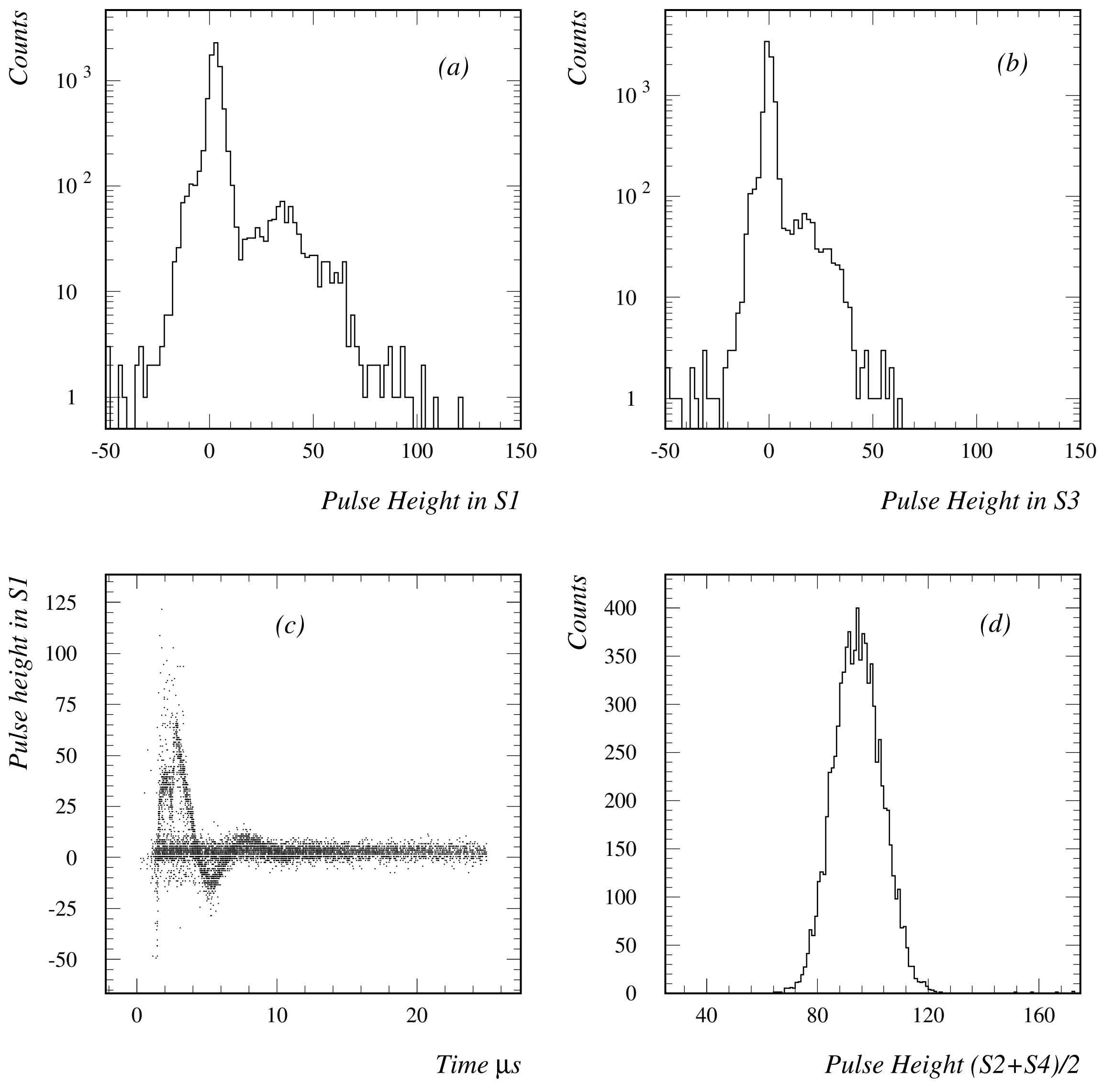

Figure 4.1: Beam scintillator system. (a) Pileup effect in veto counter S1. (b) Same for S3. (c) Pulse height in S1 vs. time after previous beam particle. (d) The average pulse height measurement by S2 and S4.

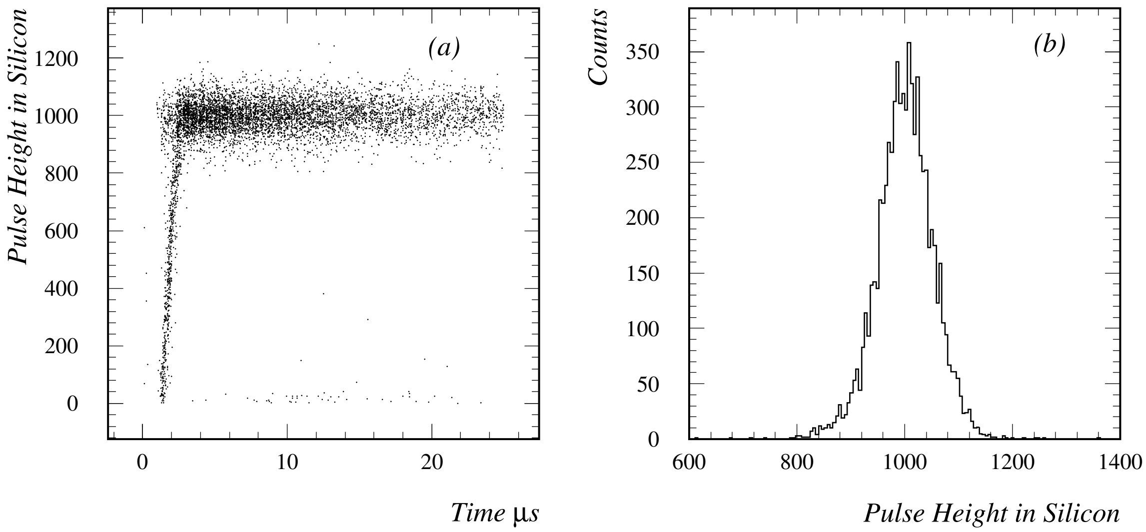

Figure 4.2: Silicon upstream detector. (a) Pulse height vs. time after previous beam particle. (b) Pulse height measurement with time after previous beam cut.

2 Data Selection

2.1 Charge Selection

After the initial interaction at the target, the heavy reaction fragments (Z/A $\approx$ 0.5) travel about 30 m before detection. Although the full flight path is filled with helium gas in order to reduce the intermediate interactions, about 30% of the heavy fragments interact, producing various nuclear fragments. Due to this reason, it is very important to measure the charge of the heavy fragments at the target and at the downstream end of the spectrometer. We use the silicon detector immediately downstream of the target to measure the charge of the outgoing fragments close to the target and the two scintillator hodoscopes (vertical and horizontal) to measure the charge at the downstream end of the spectrometer. By combining all three measurements we can easily obtain a very clean charge measurement for the heavy ion fragment.

Figure 4.3 (a) shows the measured time after previous beam particle against the measured charge at the downstream silicon detector. The pileup effect (discussed in the previous section) makes it hard to select individual charge species below 2.5 μsec. Figure 4.3 (b) shows the histogram of the measured charge distribution after applying the cut on the time after previous beam. A resolution of 4% was observed in this detector for Z=14 particles. This measurement, as it is, is not good enough to make a clean charge identification.

Figure 4.4 (a) shows a scatter plot of the measured charge in the vertical scintillator hodoscope against the measured charge in the horizontal scintillator hodoscope. The scintillator signals were corrected for the saturation effects discussed in the previous chapter. The plot indicates that the combined charge measurement from these two detectors has a better charge separation than the individual measurements. Figure

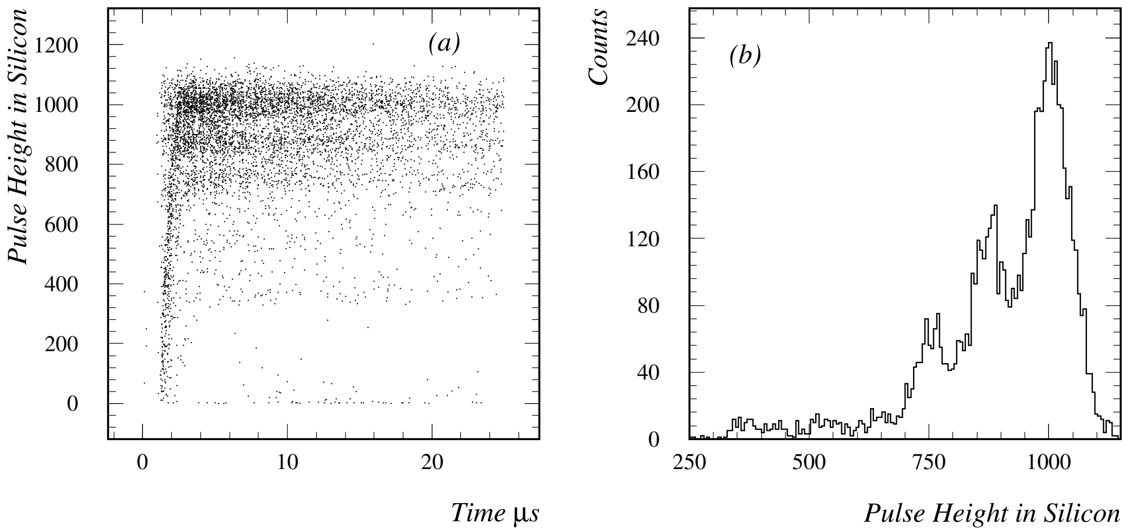

Figure 4.3: Silicon downstream detector. (a) Pulse height vs. time after previous beam particle. (b) Pulse height measurement with time after previous beam cut.

4.4 (b) shows the histogram for the combined charge measurement (double charge measurement). A resolution of 3% was obtained by this method.

Figure 4.4 (c) shows the charge measured at the silicon detector against the double charge measurement at the downstream end of the spectrometer. The horizontal band of events corresponds to the events that originated as Z=14 but interacted before reaching the downstream end of the spectrometer, producing some other charge species. In order to make a clean charge identification, hexagonal shaped gates (cuts) were made on each island that corresponded to a different charge species. The events that belong to each island correspond to three independent charge measurements. Figure 4.4 (d) shows the final triple charge measurement. Using this combination we were able to obtain a resolution of approximately 2% for Z=14 particles.

Events that fell into any of the hexagonal gates from Z=8 to Z=14 were selected as good events and the rest were discarded. Charges Z$\leq$7 were unusable due to the trigger cut at Z=7.

2.2 Event Classification

The basic criteria for selecting EMD events is based on the assumption that the electromagnetic processes do not produce any activity at the target region. The projectile will essentially travel along its path without interacting, with the exception that it gains some additional energy by the absorption of a virtual photon. This excess energy may be enough to allow ejection of one or more nucleons from the nuclei. Nuclear collisions on the other hand are hard collisions that produce particles (eg. pions) at larger angles, and they can be detected by the target region detectors.

The background to the electromagnetic process can come from very soft nuclear

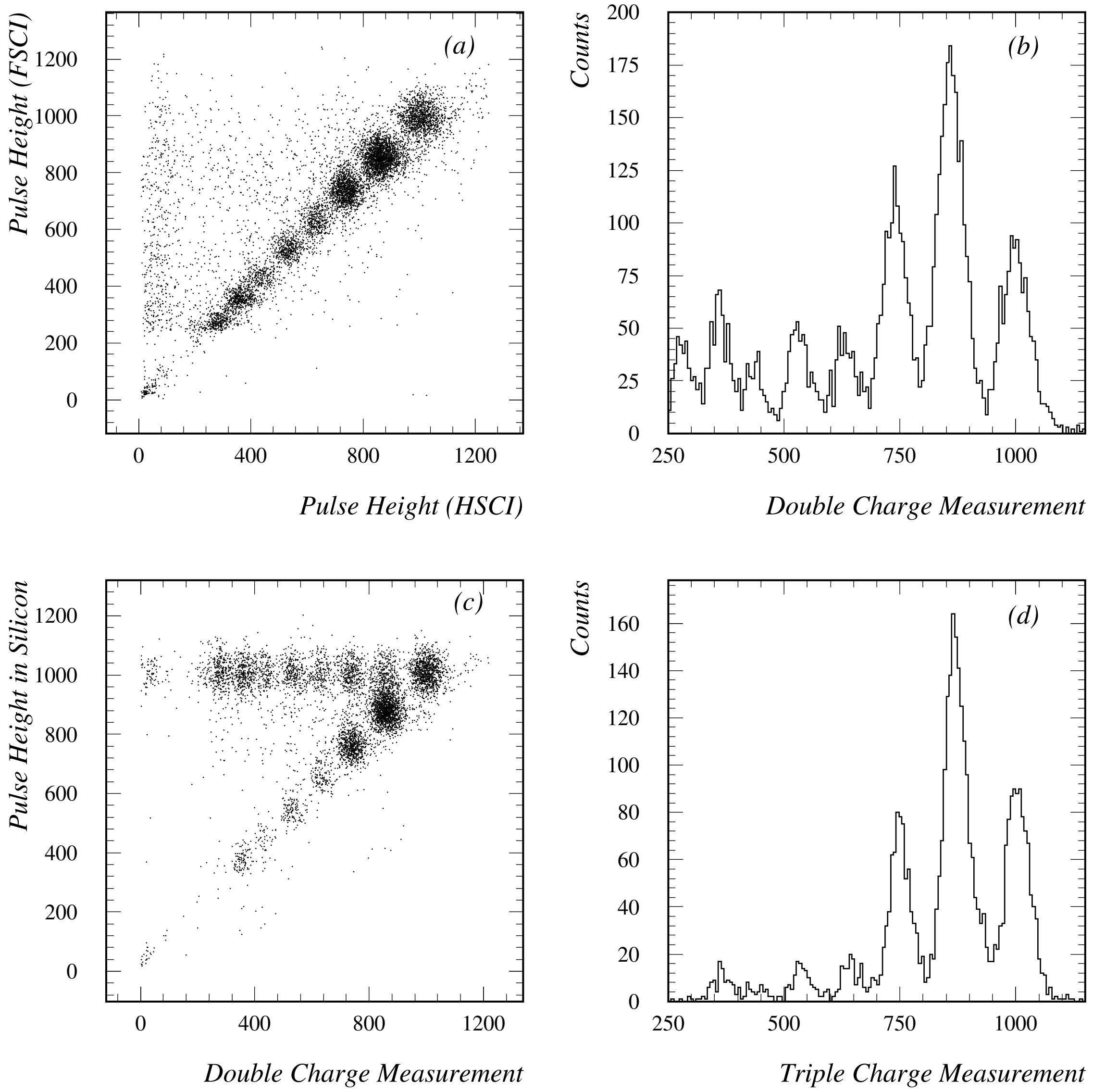

Figure 4.4: Triple charge measurement. (a) Pulse height in FSCI vs. pulse height in HSCI. (b) Double charge measurement by FSCI and HSCI. (c) Silicon downstream detector vs. double charge. (d) Triple charge measurement by combining all three measurements.

fragmentation which produce the same final state products as the electromagnetic processes and also have no activity in the target region. These processes cannot be distinguished from the EMD process on an event by event basis, but can be separated by studying the Z and A dependence of the dissociations. Selection criteria were developed to minimize the nuclear background, while keeping a high efficiency for EMD events.

The basic selection criteria was defined by studying the background as well as the target region activity produced by pure beam particles. The pure beam particles were identified by selecting the Z=14 particles that entered the experiment through the beam scintillator system and the upstream silicon detector system. Requirements were then imposed to select only the events which survive as ^{28}Si, by measuring the charge and the energy at the downstream end of the spectrometer. A pure electromagnetic interaction does not produce more activity than a pure beam particle that passes through a given target without any interaction.

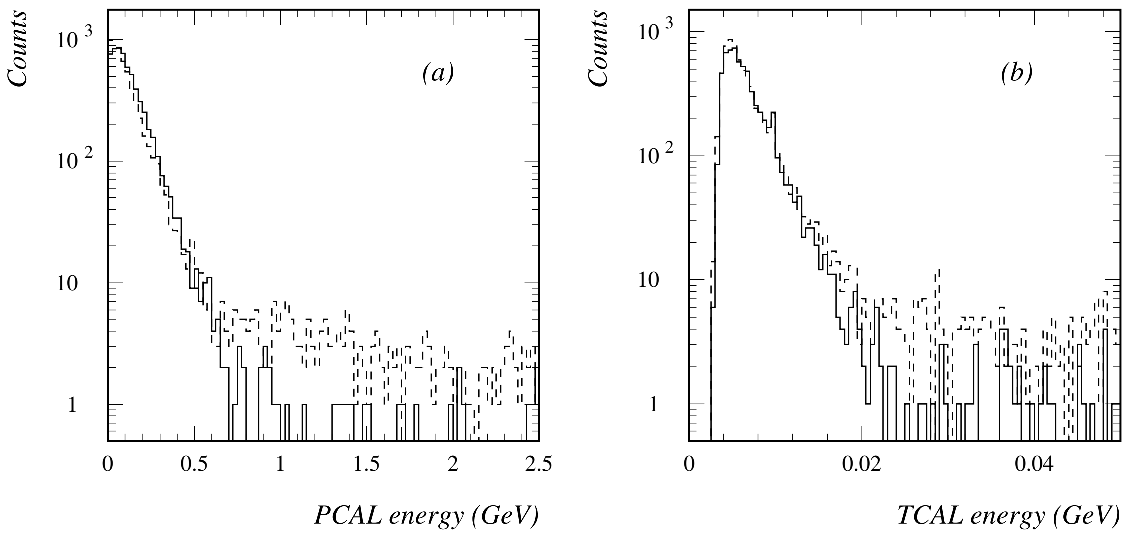

Figure 4.5: EMD event selection. (a) Energy measured in the PCAL for non-interacting beam events (solid line) and normal peripheral events (dashed line). (b) Same for TCAL.

Figure 4.5 (a) shows the total energy measured in a participant calorimeter for Si beams passing through a Pb target. The solid curve is for selected good beam tracks. The dashed curve is for normal peripheral triggers. Figure 4.5 (b) shows the maximum energy seen in any of the crystals in the side walls of the target calorimeter for the same type of events. Both of these spectra show a higher energy tail originating from non-peripheral interactions.

The response of each detector system was studied for selected good beam events and peripheral events by generating plots similar to those shown above. The cuts were imposed at each detector to reject $\leq$1% of the good beam events. The selected cuts are listed in Table 4.3.

Table 4.3: List of cuts used in EMD selection. The events which produce energy and multiplicity below the values listed here for each detector were taken as good peripheral events.

Detector System	Cut Description	Cut
Multiplicity Detector	Charge Multiplicity	25
Target Paddles	Charge Multiplicity	4
Target Calorimeter	Maximum energy in side walls	20 MeV
	Maximum energy in back wall	15 MeV
Participant Calorimeter	Maximum energy in EM section	200 MeV
	Maximum energy in HD section	200 MeV
	Total Energy	1 GeV
Magnet Scintillators	Charge Multiplicity	5
Pi-neut Calorimeters	Maximum tower energy	0.5 GeV
Neutron region scintillators	Charge Multiplicity	3

Good electromagnetic events are defined as events which do not produce an energy or a hit multiplicity above the cuts listed in Table 4.3, in any of the detectors. Events which produce any activity above these cuts in one or more of the detectors are taken as events originating from nuclear interactions. The additional information about the electromagnetic or nuclear origin was recorded in the secondary 8 mm tapes with the original data records to be used in further studies.

Table 4.4 shows the efficiency of the cuts for different targets when applied together on selected beam particles. The rejection could be due to the accidental δ rays, or the noise problems in the detector systems.

Table 4.4: Estimated efficiency in the offline selection procedure for selecting events produced by the electromagnetic interactions for various targets.

Target	Efficiency %
Pb	96.2 ± 0.5
Sn	95.7 ± 0.2
Cu	95.9 ± 0.5
Al	97.0 ± 0.4
C	–
MT	96.8 ± 0.6

No target dependence of the overall efficiency was observed and hence the same cuts were applied to all targets for the selection of electromagnetic interactions.

C Cross Sections for Simple Channels

The simplest analysis topic of the peripheral collisions is the cross section measurements. Among cross sections, a single proton (1p) or a single neutron (1n) emission cross sections are the simplest and they provide a unique way to estimate the efficiency of the selection procedure. In this section, a detailed description of the cross section estimates for these two channels are given.

1 Event Characterization

After extracting the events that originate from electromagnetic interactions, the next step is to identify simultaneously all the fragments leading to the final state in question. This was done by measuring the charge and the energy of the reaction fragments. The drift chambers were not used for the identification of 1p and 1n emission channels.

1.1 Charge Measurement

The charge of the heavy ion provides the information about the missing number of protons. For example, for 1p emissions our measurement should be the charge of ^{27}Al, which is Z=13 or for 1n emissions it should be the charge of ^{27}Si which is Z=14. Hence, a tight requirement on the charge of the heavy ion could remove most of the background for the channel in question.

The triple charge selection described in the earlier section gives us a very clean charge measurement for the heavy fragment. Figure 4.6 (a) shows the measured charge spectra at the downstream silicon detector for selected Z=14, Z=13 and Z=12 charge fragments with the triple charge selection. The plot demonstrates our ability to select portions of each charge species even in the overlapping regions. Although the downstream silicon detector measurement does not provide a clean charge separation by itself, this, combined with the vertical and horizontal scintillator hodoscope measurements gives an extremely good charge measurement.

In addition, the total charge in the upstream forward scintillators (upstream charge sum) was used to identify the protons deflecting into the Z/A=1 region. Figure 4.6 (b) shows the upstream charge sum for peripheral events. In this plot, peaks corresponding to one or two Z=1 particles are clearly visible. Only a loose cut at the lower edge was used since the charge spectrum has higher pulse heights due to the energy loss mechanisms in the scintillators (Landau shape) and the production of δ rays in the two drift chambers quite close to the upstream forward scintillators. The δ rays were mainly produced when the heavy ion tracks passed through the drift chambers. This effect was more prominent in the counters close to the beam line.

1.2 Energy Measurements

The energy in the proton and neutron calorimeters provide the additional information that is necessary to remove the background in these two channels. Figure 4.7 (a) is a

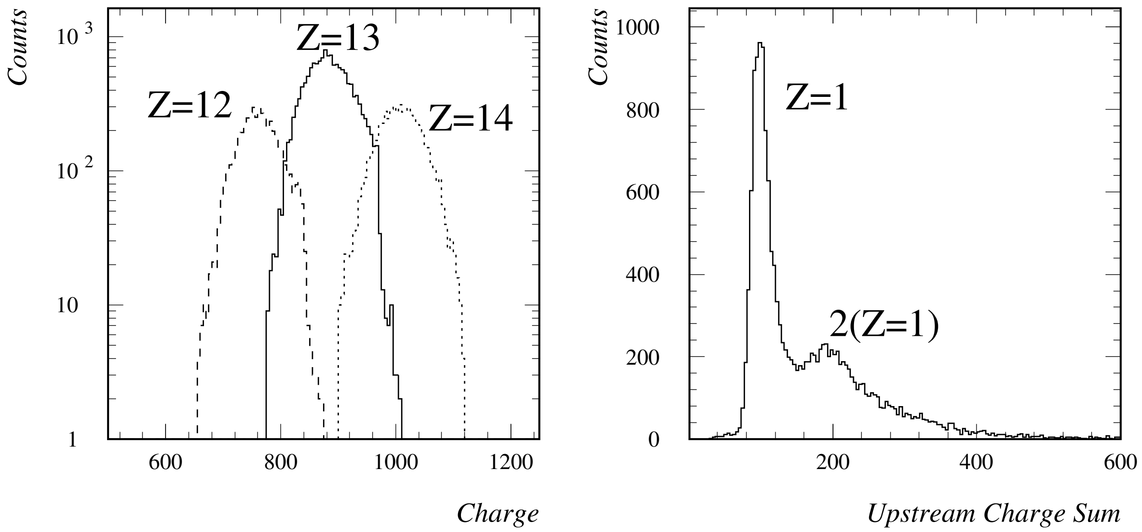

Figure 4.6: Charge selection. (a) Measured heavy ion charge for Z=14, Z=13 and Z=12 fragments. (b) The total charge measured in the upstream FSCI.

scatter plot of the raw energy in the proton calorimeters verses the raw energy in the neutron calorimeters for selected Z=13 and Z=14 particles. Three different clusters are visible in this plot. They are the protons and neutrons created by 1p+^{27}Al, 1n+^{27}Si and 1p+1n+^{26}Al reactions. It is clear from this plot that with extra cuts on the energy measurements we can select clean event samples for 1p and 1n emissions.

Figure 4.7 (b) shows the measured proton cluster energy for selected Z=13 candidates. A single cluster was selected as having energy between 4 and 22 GeV. A similar energy distribution was observed with neutrons for selected Z=14 candidates. Table 4.5 shows the cuts used to identify 1p and 1n emission channels.

Table 4.5: List of cuts used to select 1p and 1n events. These cuts were imposed on selected EMD event samples. The upstream charge sum was calibrated to place the minimum ionizing particles at 100 units.

Measurement	1p+^{27}Al	1n+^{27}Si
Heavy ion Charge	Z=13	Z=14
Proton Energy	4<E<22	E<4
Neutron Energy	E<4	4<E<22
Upstream Charge sum	Z_{sum}>25	–

1.3 P/Z from Scintillators

Although we do not need to measure P/Z of the heavy fragment to identify the 1p or 1n channels, the horizontal scintillator hodoscope provides confirmation of the purity

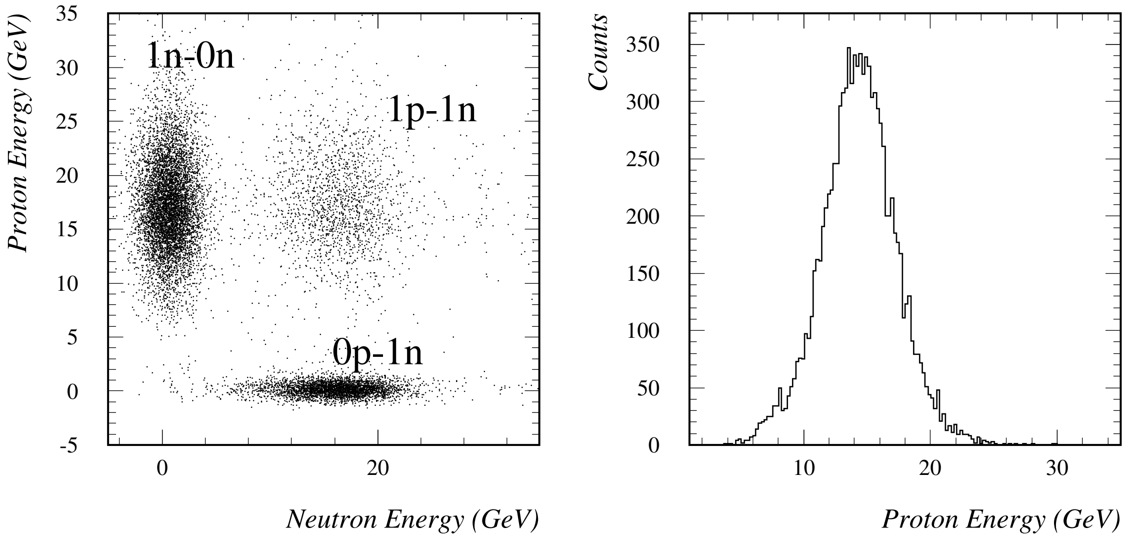

Figure 4.7: Energy selection. (a) Energy in the proton calorimeter vs. the neutron calorimeter for Z=13 and Z=14 events. (b) Proton calorimeter energy for selected 1p events with Z=13 and cut on neutron energy.

of the samples. The position of the heavy fragment in the horizontal scintillator hodoscope corresponds to the P/Z of the heavy fragment. Figure 4.8 shows the position distributions obtained for selected 1p, 1n, 1p1n and 2p channels. The position resolution of the horizontal scintillator hodoscope is about 2 cm. The distributions are corrected for the beam angle variations measured by the beam vertex detector. No cuts were applied based on this measurement due to the large variations in the position measurements arising from the gain drifts in the phototubes and the many overlaps between different channels. However, the P/Z estimations obtained through drift chamber track reconstruction turn out to be an extremely useful tool in selecting more complex channels. Such measurements are discussed later in the thesis.

2 Cross Section estimates

2.1 Efficiencies

Before estimating the absolute cross sections there are a number of corrections that need to be extracted from an unbiased data sample. These corrections arise from inefficiencies introduced by the selection procedures. The correction factors are evaluated carefully using pre-trigger and beam trigger data in such a way that the same efficiency is not counted twice.

The methods used to estimate the efficiencies are described below. A list of estimated efficiency factors obtained by this method is given in Table 4.6.

- *Upstream Interactions* – The upstream interaction efficiency was calculated by estimating the number of beam particles that were selected by the beam trigger

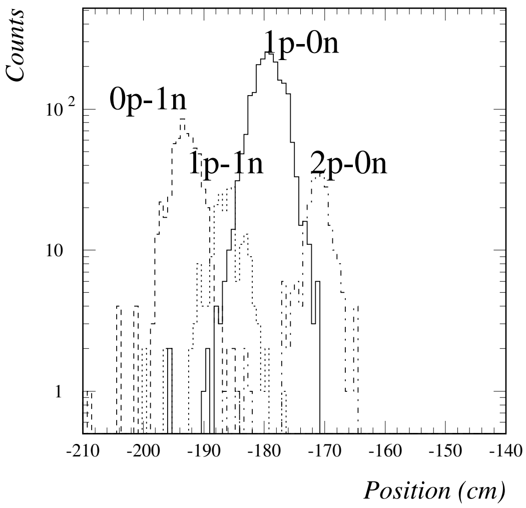

Figure 4.8: Measured position of the heavy ion fragments at the downstream horizontal counter for selected channels.

but were rejected by the cuts used in the beam scintillators and the upstream silicon detector. This represents the efficiency in the trigger of detecting good beam particles. The contribution of the time after previous beam cut at 2.5 μsec was not included in this but was calculated as a separate efficiency.

- *Downstream interactions* – The downstream interaction efficiency was calculated by selecting a sample of known Z, defined by the downstream silicon detector and the upstream proton calorimeters using low level triggers (beam triggers or pre-triggers). The probability of detecting the selected isotope inside the gates used in the triple charge measurement directly provides the downstream interaction efficiency. As a result, the cracks between individual scintillators, inefficiencies in selected gates etc are also included in the estimation. This efficiency in principle has a Z dependence.

- *Veto wall* – The veto wall efficiencies were estimated with a sample of Z which was already identified as good events with no downstream interactions, using the pre-trigger tapes. The probability of the survival of these events with and without the veto wall selection gives us the efficiency of this cut. It was assumed that this cut does not depend on the Z of the isotope or on the type of target, although there could be a small dependence due to the production of δ rays.

- *Proton and Neutron Clusters* – The clustering algorithms fail to predict the correct energy for nucleons going through the cracks or gaps in calorimeter modules. In addition, shower fluctuations could lead to some inefficiency due to a low energy deposition. The efficiency arising from clustering algorithms was estimated by selecting a known sample of 1p and 1n events in the pre-trigger sample which produces energy outside the applied cuts in the analysis for these calorimeters.

- *Upstream Charge Sum* – The efficiency due to the upstream charge sum was calculated by selecting a good sample of 1p events without using the upstream charge sum, but using all other available detectors. The inefficiency of this cut arises due to the gaps between scintillation plates.

- *Downstream silicon detector* – The efficiency in the downstream silicon detector was calculated by selecting Z=14 particles from the upstream silicon detector and the downstream forward scintillator measurement. It was necessary to select the Z of the fragment at the downstream end of the spectrometer since a clean sample with a known Z was needed to estimate this efficiency. It was assumed that all gates defined to select different charges have the same efficiency.

- *Offline veto* – The offline veto efficiency was taken as the average of the efficiencies calculated for each target, with and without the offline vetos, using selected good beam tracks. Although cuts on each detector measurement were limited to reject only upto 1% of the good beam particles, when applied together, they produce a non negligible effect. The individual efficiencies for each target are listed in Table 4. Although a target dependence in this efficiency was anticipated, we have not observed one.

- *Time after previous beam* – The efficiency due to time after previous beam cut was evaluated by estimating the number of surviving good beam particles with and without the 2.5 μsec cut. The rejection due to this cut showed a large variation among the runs and hence was calculated separately for each run. Only the average value is shown in Table 6. It was found that the pileup effect for the latter part of the data tapes was low and therefore a somewhat lower (2.2 μsec) cut was applied for these data.

- *On-line veto detectors* – To evaluate the on-line veto efficiency, the same analysis was applied to the events taken with veto and the events taken without the veto requirements. The ratio of the yields of these two samples, with proper normalization for the trigger downscaling, provided the required efficiency. To reduce the fluctuation due to low statistics, for each run, the ratio was weighted with the average formed separately for each trigger by the trigger scaler counts. It was found that this efficiency is strongly target dependent.

Due to their run dependence,the efficiencies for the time after previous beam and on-line veto detectors were estimated on a run by run basis. Only the average is shown in Table 4.6. The large inefficiency in the neutron cluster energy selection compared to the proton cluster energy selection is probably due to the cracks in the neutron calorimeters located in the zero degree line. The pre-trigger efficiencies for 1p and

Table 4.6: List of efficiencies for the cuts used to select 1p and 1n events. These efficiency factors can be considered as independent of each other.

Selection Criteria	Efficiency %
Upstream interactions	97.8 ± 0.2
Downstream interactions	70.6 ± 1.9
Veto wall selection	87.5 ± 1.8
Proton clusters	95.8 ± 1.0
Neutron clusters	90.0 ± 2.0
Upstream charge sum	95.1 ± 0.6
Downstream silicon detector	98.0 ± 0.3
Offline veto detectors	96.3 ± 0.5
Time after previous beam	86.2 ± 2.2
On-line veto detectors	76.9 ± 1.4

1n are found to be 100%. We estimate the total efficiency [1] for 1p and 1n detection as 34%. This number is obtained by taking the product of all the relevant efficiency factors for each trigger type listed in the Table 4.6, assuming that the efficiency factors are independent from each other.

2.2 Cross Sections

The following formula was used to calculate the exclusive cross sections;

$$\sigma = \left(\frac{N}{B}\right)\left[\frac{MD}{N_A W_t}\right]\left(\frac{1}{f}\right) \tag{4.1}$$

where M is the atomic weight of the target material, D is the downscaling factor, N_A is the Avagadro number, W_t is the target thickness in g/cm^2, f is the efficiency factor, B is the total number of beam particles and N is the observed number of events for any given channel. A list of the targets used, and their properties are listed in Table 4.7.

The total number of beam particles extracted from the beam scalers were corrected for the loss of events due to after protection. This was done by estimating the number of beam particles that were rejected, by using the recorded number of pre-triggers rejected by the first level trigger. This has approximately 10% effect on the cross section estimates and cannot be neglected.

[1] Note that the total efficiency estimated for 1p events is slightly lower than the values given in Ref [31]. This is due to the fact that the efficiency of the offline veto detectors were not accounted for in the reference. Therefore, the cross sections and the other parameters extracted from the 1p data given in this thesis are slightly different to the values given in Ref [31].

Table 4.7: List of targets and their properties.

Target	Atomic weight M	Charge Z	Thickness W_t (g/cm^2)
Pb	208	82	4.359
Sn	120	50	3.253
Cu	64	29	2.239
AL	27	13	1.300
C	12	6	0.596

The observed number of counts were corrected for the interactions due to air, helium, or any other material in the path, by normalizing the counts observed for the empty target frame to the total number of beam particles used. The empty contribution for Pb and C targets are 5% and 50% respectively. In addition, part of the data obtained from 1n triggers were corrected for a trigger problem which affected 50% of the total 1n sample. This was caused by a failure of a signal cable used in the 1n trigger to detect neutrons in one U/Cu calorimeter module. The estimated correction factor for this is about 30% on the cross section values obtained by the 1n trigger.

Since the downscaling factor depends on the type of trigger used, the cross sections were calculated separately for each trigger. The evaluated cross sections for 1p and 1n channels are listed in Table 4.8. The errors include the statistical and the observed run to run variations. We estimate an additional systematic uncertainty of the total cross section values of approximately 5%. For comparison, earlier measurements of cross sections with the E814 apparatus [31] are listed. A good overall agreement is seen although the two sets of data are quite different.

Table 4.8: Measured cross sections for 1p and 1n emission by EMD. For comparison, earlier cross section measurements through our experiment are also listed.

Target	1p cross sections (mb)		1n cross sections (mb)	
	This work	Ref [31]	This work	Ref [31]
Pb	676.4±33.5	672.2±24.8	241.0±13.1	268.5±12.0
Sn	274.0±14.6	290.6±13.8	100.0± 4.5	103.2± 7.1
Cu	111.0± 2.2		40.4± 4.8	
Al	31.6± 3.6	34.2± 4.7	13.1± 1.8	11.3± 2.3
C	13.3± 0.7		6.3± 0.4	

CHAPTER 5

Reconstruction of Events

This chapter explains the methods developed to reconstruct the simple decay channels that have two or three particles in the final state. A complete event reconstruction was carried out by constructing the track segments at each detector and successively combining them with geometrical and kinematical constraint fits which exploit the physics behind the reaction under investigation. The methods discussed here are quite general in nature and can easily be extended to study other reactions.

A Track Reconstruction

The tracks in the forward spectrometer are reconstructed by performing a crude selection, followed by a detailed pattern recognition. The information from the detectors which measure the position of the particles upstream and downstream of the magnet are combined to obtain track parameters such as the position and the angle along the path of the particles as well as the magnetic rigidity P/Z.

1 Preliminary Selection

The preliminary extraction of tracking information was carried out by selecting possible hit candidates that are generated by the passing tracks at the beam vertex detector, the pad chamber DC1, the drift chambers DC2 and DC3, the forward scintillators and the U/Cu calorimeters. The detailed analysis described in chapter 3 was performed to eliminate noise and to construct the possible hit candidates at each detector plane.

For peripheral events, it is necessary to identify tracks that belong to the heavy ions and the other light fragments simultaneously. The identification of the hits which belong to the heavy ions is straightforward since, from all the possible hit candidates, these produce the highest charge or energy. This is not the case for the drift sections of DC2 and DC3 since the TDC does not carry information about the charge or the energy of the passing tracks. However, the pad sections located at the end of each chamber measure the charge of the passing tracks and these measurements can be used to initiate the selection procedure in the drift chambers.

The pattern recognition in the drift chambers was carried out by establishing "roads" in the drift and pad sections to identify the track segments within each chamber. These roads are defined to an accuracy of the width of the pads, which varies over the pad plane. The possible variation in the angle of the tracks for peripheral events crossing each chamber at different locations was also incorporated in establishing roads. No attempt was made to remove the left-right ambiguity in the x locations predicted by the TDC hits and both possibilities were kept at this stage of the analysis. The roads which contained hits in 3 or more of the 6 planes were taken as the possible hits generated by the real tracks.

The connection between the roads in DC2 and DC3, and the hit clusters in the forward scintillators generated by the same particle traversing the detectors downstream to the magnet was obtained by performing a linear least squares fit for these three measurement (both in the x and the y directions). The agreement between the calorimeter measurements and the predicted measurements (using the results of the fit and extrapolating them to the plane of the calorimeters) was used to select the best candidates to form the links between the track segments that form the tracks downstream of the magnet.

The x position in the pad chamber DC1 belonging to any track can be predicted by using the information from the beam vertex detector and the downstream crude track reconstruction combined with a simple magnet model. In this model the two magnets are replaced by two bending planes as shown in Figure 5.1. Here, x_o represents the position of the beam track at the target plane. This can be extracted from the beam vertex detector measurements. The outgoing track angle at the target plane which is represented by θ_o is very close in measurement to the incoming beam angle for the heavy ions but not for the light particles. The angle and the position of the downstream track at the plane of DC2 are represented by $\acute{\theta}$ and $\acute{x}$ respectively and the bending angles at each magnet are represented by θ_1 and θ_2 respectively.

The x position at DC1 is related to the upstream and downstream information by the formula,

$$x_{DC1} = x_1 + (x_2 - x_1) \times \left[\frac{z_{DC1} - z_1}{z_2 - z_1}\right]$$

where x_1 and x_2 are given by;

$$x_1 = x_o + z_1\theta_o$$

$$x_2 = \acute{x} - (\acute{z} - z_2)\acute{\theta}$$

The upstream angle θ_o can be calculated by;

$$\theta_o = \left[\frac{3(\acute{x} - x_o) - \acute{\theta}(2z_2 + z_1 - 3\acute{z})}{2z_2 + z_1}\right]$$

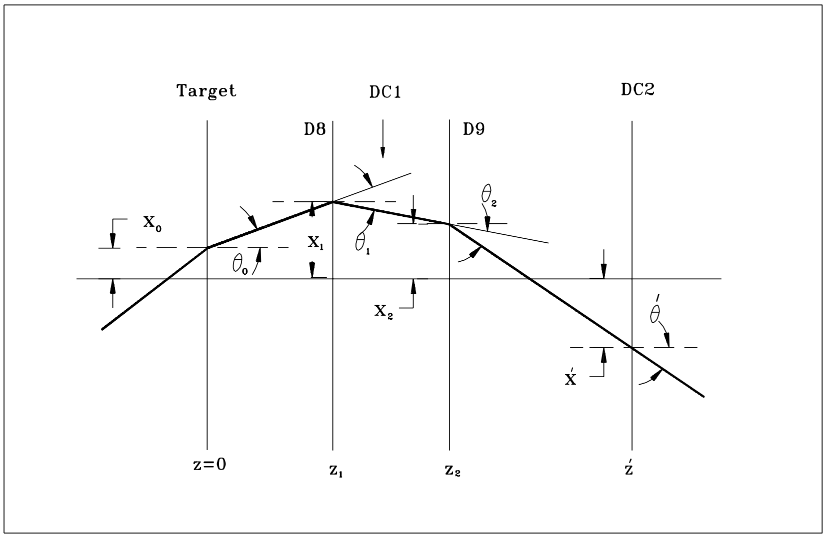

Figure 5.1: Two bend magnet model used in the preliminary analysis.

where we have taken the value of the ratio θ_1/θ_2 to be 2.0 from the magnetic field settings and effective lengths. By substituting the known values for the locations of the measuring planes along the z direction (z_1, z_2, etc) we can estimate x_{DC1}. In addition, this method allows us to calculate a crude value for the magnetic rigidity P/Z by using the simple relationship;

$$\left(\frac{P}{Z}\right) = \frac{k}{(\acute{\theta} - \theta_o)}$$

where k is a constant found to be ≈ 1.85. The value of P/Z extracted by this method was used to solve various software problems at the early stages of the peripheral analysis.

Figures 5.2 (a) and (b) show the difference between the predicted and the measured x positions at DC1 for heavy ions and protons respectively. The plots indicate our ability to select hits in DC1 without using time consuming pattern recognition algorithms. For the y agreement, a direct extrapolation was used by assuming that the tracks pass $y = 0$ at the target plane. The hits in DC1 were identified by searching for the best candidate in the neighborhood of the predicted x and y positions.

All the possible hits in DC1, DC2, DC3 (both drift and pad sections), the forward scintillators and the calorimeters, along with the hits in the beam vertex detector were passed on to our pattern recognition program (GRIST) which was developed to perform full event reconstruction in the peripheral analysis.

2 Pattern Recognition in Drift Chambers

The most tedious pattern recognition in E814 tracking chambers involves reconstructing the tracks in the drift sections. This is complicated by the ambiguity in the posi-

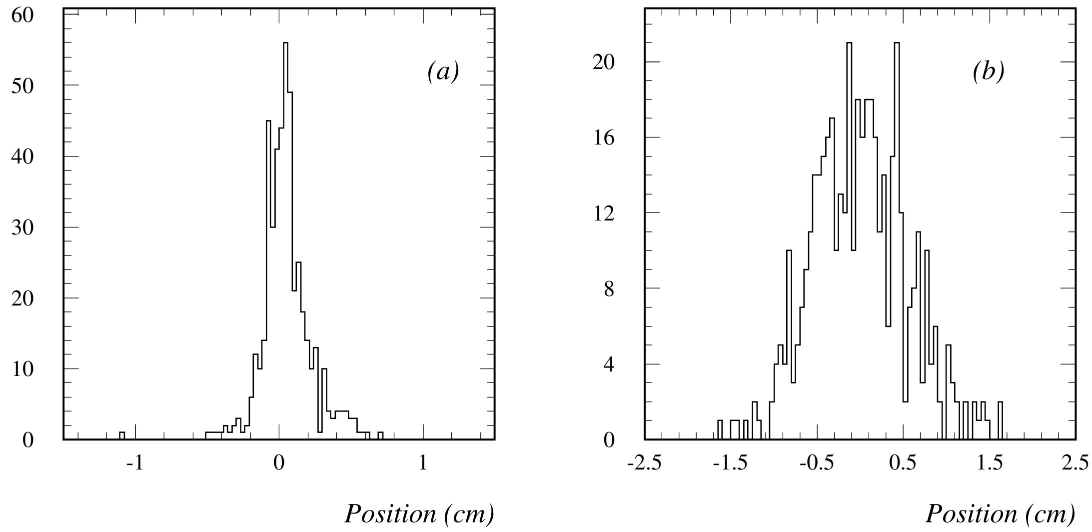

Figure 5.2: Accuracy of the DC1 hit selection. (a) Difference between the predicted and measured heavy ion positions. (b) Same for protons.

tions generated by the TDC hits which could be on either side of the anode wires, as well as the δ rays generated by the passing charge particles. For the heavy ion tracks, the rejection of the TDC hits created by the δ rays is the major problem.

It was found that the sum of the drift times of charge clusters drifting in opposite directions of neighboring anode wires provides a good selection criteria for the selection of true TDC hits originating from the passing tracks. Hits created by the δ rays do not produce the correct drift times that are produced by the good TDC hits which originate from the charge clouds. However, depending on the position of the tracks traversing between the neighboring planes which are shifted by half a cell relative to each other, the sum of the drift times varied by an amount that is proportional to the angle of the tracks. A correction was made to remove this effect in neighbor sums by estimating the angle of the tracks, using the pad locations reported in DC2 and DC3 by the preliminary selection procedures described earlier. Figures 5.3 (a) and (b) show the neighbor sums for heavy ions and protons passing through DC2 respectively. A FWHM of $\approx$ 30 and 60 ns were observed for DC2 and DC3 respectively.

By requiring that the sum of the drift times obtained from the neighboring anode wires fall within a window that corresponds to $\pm$ 1.0 mm in space, consistent hits within DC2 or DC3 were identified in the track reconstruction stage. Centroids were formed with the hits that satisfied this criteria and were observed in the odd-even planes. The location of the set of drift chamber hits which were most consistent with a straight line segment falling within the road was obtained using the Principle Component Analysis [56]. The left-right ambiguities are eliminated by the use of such centroids. After identifying the correct TDC hits, the centroids were discarded and the original TDC values were used in the track construction.

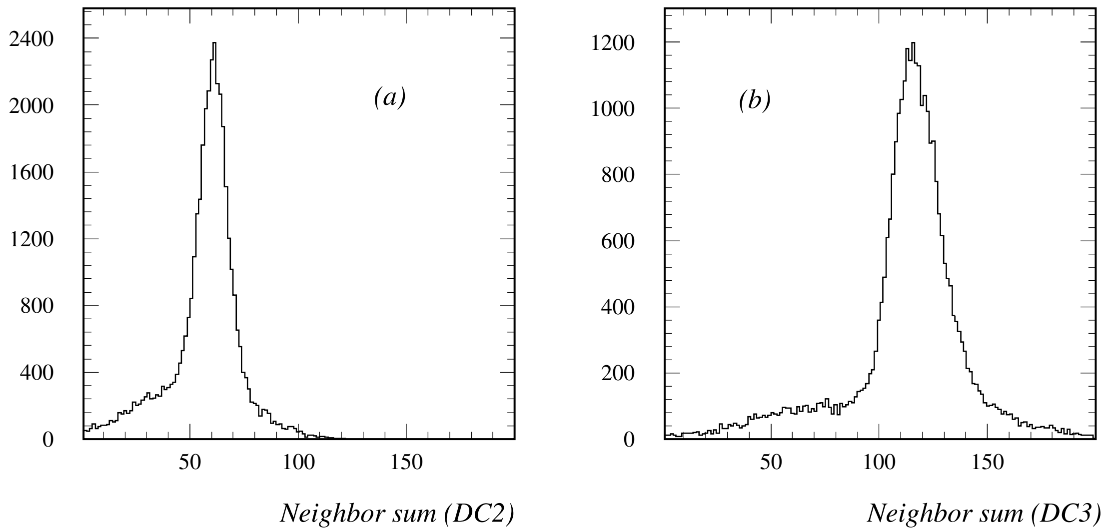

Figure 5.3: Measured sums of drift times in neighboring anode wires for protons. (a) DC2. (b) DC3.

The facility to obtain high level TDC hits [1] or so called second TDC hits, is incorporated mainly to help separate the hits generated by δ rays from the true charge clouds. Figure 5.4 (a) shows the second hit against the first hit measured for beam tracks passing through one plane of the chamber DC2. As expected, a majority of the events show a good correlation between these two measurements. But, an additional correlated band which is shifted by 40 ns or so from the main band was observed. Detailed studies showed that in some isolated cases, not one, but several of these could be observed even for individual wires. One explanation could be that the arriving charge clouds contained several peaks in the TDC distributions due to the distortion from δ rays and therefore the zero crossing discriminators were firing several times for the same charge cloud, with different time intervals. However, this did not complicate the analysis described in this thesis since the second hits were not used in the primary selection. Figure 5.4 (b) shows the same events after selecting the best events through our selection criteria. The second band is observed less frequently now, indicating that it consists mainly of hits distorted by the δ rays. To identify a set of good TDC hits, the initial pattern recognition was started with those hits which reported second hits.

For the charged particle tracks, the position information from the forward scintillators and the calorimeters was not used in the final track reconstruction stage. It was used only to guide the initial pattern recognition since the drift chambers provided a better resolution. However, to reconstruct neutral particles (neutrons), the calorimeter position and energy information were used since these were the only available information for these particles.

[1] see chapter 3, section 2.4

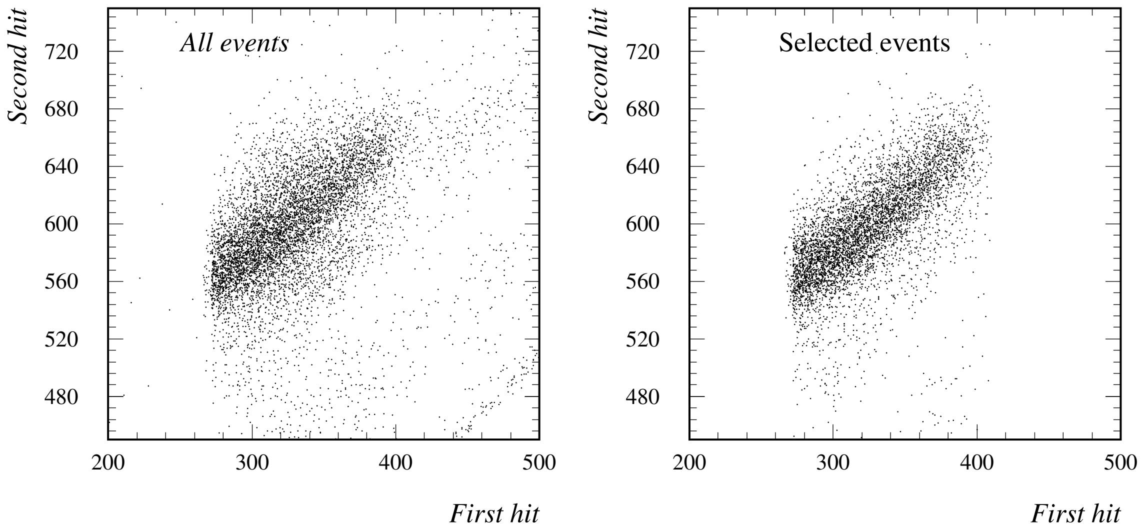

Figure 5.4: Second TDC hit vs. the first TDC hit. (a) All hits. (b) Selected hits.

3 Tracking Details

3.1 Detector Alignments

Using the hits identified in the previous step, a fit was performed on the drift time values measured in DC2 and DC3, the horizontal and vertical positions identified in DC1, and the vertical positions found in the cathode pad sections of DC2 and DC3. Because of the inaccuracy in the vertical measurements, the track is constrained to pass through y=0 at the target. The vertical distribution of the beam particles is approximately gaussian, centered at y=0 with FWHM $\approx$ 6 mm. Since the trajectory passes through the magnet, the value of the magnetic rigidity for the track is introduced as a variable in this fit, along with the horizontal and vertical slopes and the intercepts of the tracks at the position of the target.

It was found that the physical locations of the detectors measured by surveyors are not accurate enough to obtain an optimum resolution from these chambers. The following steps were carried out to align the detectors. The results obtained for the x alignments of the tracking detectors are listed in Table 5.1. A similar procedure was carried out to align the detectors in the y direction.

- By using the given survey measurements, the beam tracks (with no target in the target holder) were reconstructed and the magnetic rigidity P/Z was measured. This value was taken as the true P/Z of the beam tracks, assuming that the offsets in the survey measurements were random and therefore did not cause any systematic change in the reconstructed P/Z value.

- By using the measurements reported by the first plane of the beam vertex detector and the drift chamber DC3, the beam tracks were reconstructed with

Table 5.1: List of offset constants extracted by the alignment studies.

Detector description	z Position (cm)	x Offset (cm)	Resolution (mm)
DC1 pad plane x	398.573	-0.038	0.200
DC2 wire plane 1	687.073	-0.097	0.300
DC2 wire plane 2	687.708	-0.070	0.300
DC2 wire plane 3	688.343	-0.074	0.300
DC2 wire plane 4	688.978	-0.067	0.300
DC2 wire plane 5	689.613	-0.062	0.300
DC2 wire plane 6	690.248	-0.072	0.300
DC3 wire plane 1	1158.164	0.020	0.300
DC3 wire plane 2	1159.434	0.030	0.300
DC3 wire plane 3	1160.704	0.044	0.300
DC3 wire plane 4	1161.974	0.030	0.300
DC3 wire plane 5	1163.244	-0.005	0.300
DC3 wire plane 6	1164.514	0.045	0.300

the measured value of P/Z (extracted in the previous step) kept as a constant. The value of the shift in each detector plane (which was not used in the fit) was estimated and corrected.

- The previous step was repeated by using all the detectors other than DC3, and the offset constants were obtained for DC3. The position of the first plane of the vertex detector was assumed to be correct. This assumption did not produce any bias in the track reconstruction since all the detectors were aligned relative to the initial configuration.

3.2 Resolution in Drift Chambers

The tracking chambers were designed to detect minimum ionizing particles as well as heavy fragments. The study of peripheral interactions requires that the tracking chambers respond to both types of particles with high precision. Our pattern recognition methods indicate that the horizontal spatial resolution in each drift chamber plane for both type of tracks is $\approx 300\ \mu$m, although the heavy ion tends to produce more δ rays than the protons.

Figures 5.5 (a) and (b) show the residuals obtained for ^{27}Al tracks and proton tracks in DC2 respectively. The residuals were obtained by taking the difference between the fitted track and the measured positions. The plane to be tested was not used in the fit. In DC3 a position resolution similar to that for DC2 was achieved. Detailed studies indicate that individual wires show 100-250 μm single cell resolutions.

The reduced resolution for a single plane consisting of combining information from many wires could arise from the wire to wire offsets in these chambers.

An attempt was made to utilize the alignment method discussed above to determine individual wire offsets in the heavy ion region. Although the preliminary results were promising, the wire offset constants were not used in this analysis since this work is not yet completed and the methods involved are still under investigation.

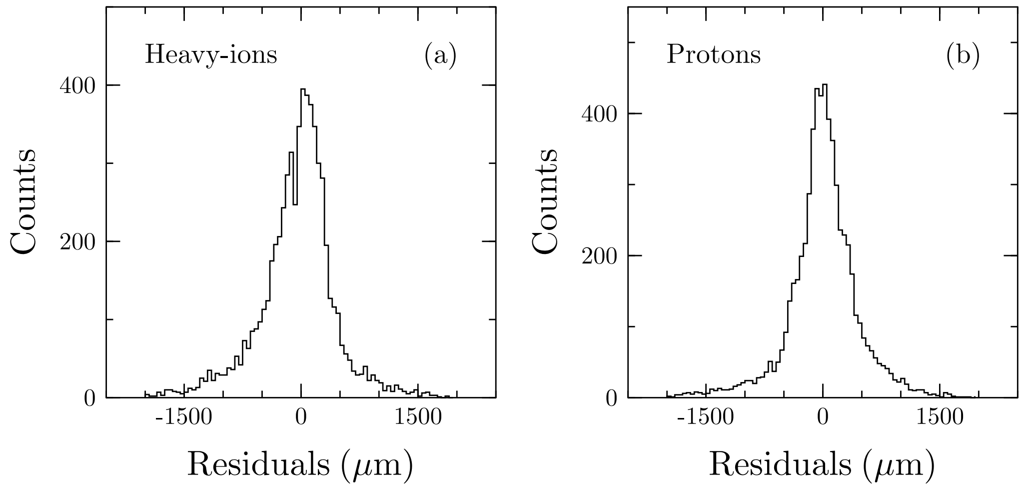

Figure 5.5: Resolution in the drift chamber DC2 (a) Heavy ions (b) Protons.

Figure 5.6 shows the measured P/Z for the beam tracks. A χ^2 cut was applied to remove the badly reconstructed tracks. A resolution of 1% was observed for the P/Z reconstruction. The major width in this distribution arises from multiple scattering in the material along the path of the track. An additional contribution of 0.25% comes from the momentum spread in extracting the ^{28}Si beam from the AGS. The value of the beam momentum extracted in this analysis was found to be 14.35$\pm$0.21 GeV/nucleon which is slightly lower than the beam momentum value of 14.6 GeV/nucleon advertised by the AGS.

B Reconstruction Studies

The improved estimates of the track variables as well as the physical quantities which we need to measure were extracted by using a reconstruction program which exploits geometrical and kinematical constraints. These constraints allow us to combine the tracking information in an optimal way to determine the parameters of interest.

1 Method of Reconstruction

The reconstruction program used in this analysis (GRIST) was originally developed at CERN during the late 1960's in an experiment which used optical spark chambers.

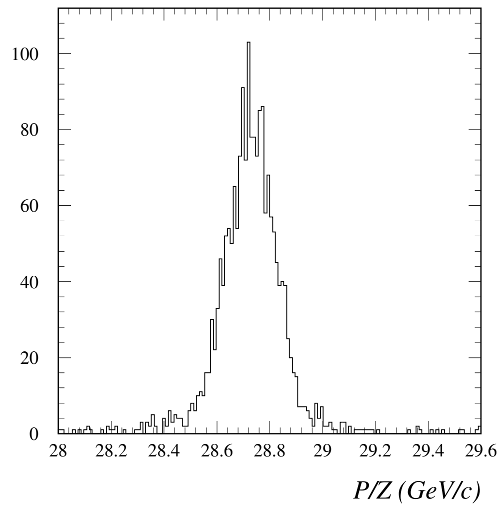

Figure 5.6: Reconstructed momentum distribution for beam particles.

This was later used in other experiments to study various reactions successfully and was modified by W.E Cleland to fit the peripheral events taken through the E814 apparatus. A brief summary of the evolution of this program is given in Table 5.2.

The method of reconstruction used in GRIST can be described as minimizing the χ^2 function with respect to a set of parameters α_j,

$$\chi^2(\alpha_j) = \sum_i \frac{1}{\sigma_i^2} \left[\xi_i - U_i(\alpha_j)\right]^2 \qquad (j = 1......n)$$

where ξ_i and σ_i represent the observations (eg. Beam vertex measurements, measured TDC values of the tracks in the drift sections of DC2 and DC3, the position measurements of calorimeters ..etc) and their precisions respectively. The U_i are the calculated values of the expected observations and are a function of the set of parameters α_j. The α_j are chosen carefully so that they can describe the given hypothesis completely. In the final kinematic fit they are related to the center of mass decay angles and invariant masses of the assumed 2-body systems which describe the process. Initially, trial values for these parameters are assigned to shorten the iterative χ^2 minimization procedure.

If α_j^o are a set of trial values for the parameters α_j, by making the Taylor expansion about α_j^o, the χ^2 to be minimized by determining the corrections $\delta\alpha_j$ can be written as,

$$\chi^2(\alpha_j) = \sum_i \frac{1}{\sigma_i^2} \left[\xi_i - U_i(\alpha_j^o) - \sum_l \delta\alpha_l \left(\frac{\partial U_i(\alpha_j)}{\partial \alpha_l}\right)\right]^2$$

Table 5.2: History of the event reconstruction code (GRIST) used in this analysis.

Years	Reaction	Ref	Features	Detectors
1965-1968	$\pi^- p \to \Lambda^o K^o \to p + \pi^-$ $p + c \to p + c$	[57]	No B field	Optical spark chambers
1968-1970	$\mu Z \to \mu\mu\mu Z$	[58]	Homogeneous B field	Optical spark chambers
1970-1973	$\Sigma + N \to \Sigma^* + N$	[59]	Inhomogeneous B field	Magnetostrictive spark chambers
1973-1976	$\Sigma^- \to \Lambda^o e\nu \to p\pi$	[60]	3 body decay (in B field)	Magnetostrictive spark chambers
1991-	$^{28}Si^* \to^{27} Al + p$ $\to^{27} Si + n$ $\to^{26} Mg + 2p$	[32]	Homogeneous B field	Drift chambers Scintillators Calorimeters etc

where $U_i(\alpha_j^o)$ are the expected values of the observation for the set α_j^o. Thus, the χ^2 minimization can be carried out by solving,

$$\delta\vec{\alpha} = A^{-1}\vec{\Delta}$$

in which

$$\Delta_k = \sum_i \frac{1}{\sigma_i^2}\left[\xi_i - U_i(\alpha_j)\right]\frac{\partial U_i}{\partial \alpha_k}$$

$$A_{lk} = \sum_i \frac{1}{\sigma_i^2}\left(\frac{\partial U_i}{\partial \alpha_l}\frac{\partial U_i}{\partial \alpha_k}\right)$$

where A^{-1} is the error matrix for the α_j and $\delta\vec{\alpha}$ is the correction done to the initially selected α_j^o to obtain the minimum χ^2.

If the expected observations U_i have a linear dependence on the α_j, then the correct result can be obtained immediately. But since this is not the case for our data (and for most cases), an iterative procedure had to be used in which the convergence was dependent on the number of parameters involved and how well the initial parameters were chosen.

2 Application to Peripheral Events

2.1 Geometrical Constraint Fitting

The event reconstruction procedure was initiated by forming the individual track segments and by successively building up the vertices. This is essentially a purely geometric fit, in which the angles of the tracks, the coordinates of the vertices, and the masses and the momentum of the particles are involved as parameters. In forming tracks in space, we need 5 parameters to specify each track (assuming that the tracks pass through magnets, since we would otherwise need only 4 parameters). They are, the x and y intercepts at the plane $z = 0$, the angles in the xz and the yz planes and the momentum of the particles associated with the given track. Geometrical constraints can be imposed according to a given hypothesis when forming the vertices for separate track segments.

Consider the example given in Figure 5.7 for the $^{28}Si^{*} \rightarrow 1p+^{27}Al$ system. The incoming beam track has only two parameters, the position and the angle at the target on the xz plane which are obtained from the beam vertex detector. The vertical information which is an unknown for our data was introduced as an additional parameter. For each outgoing track, only 3 parameters are needed since all three tracks have to form a vertex at the target. Therefore, we have a 9 parameter fit. If the three tracks were unconstrained, the pattern would be described by 2 parameters for the incoming track and 5 parameters for each of the outgoing tracks, for a total of 12 parameters. Thus, this fit has 3 geometrical constraints.

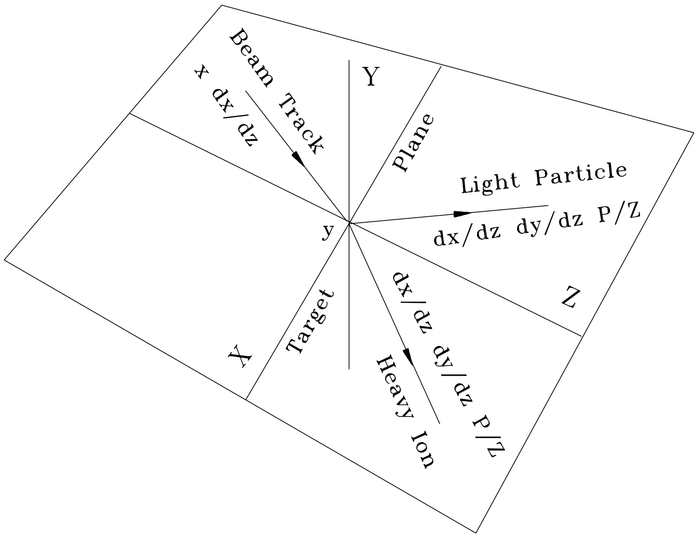

Figure 5.7: Selected geometrical parameters for the two body decay.

In the case of the $1n+^{27}Si$ system, only the measured position at the downstream calorimeters for the outgoing neutron was available to be used in the fit and hence, only a 1 geometrical constraint fit is formed.

2.2 Kinematically Constrained Fitting

The excitation energy of the projectile can be obtained by measuring the invariant mass of the system in question. Although the analysis can be carried out for systems with several nucleons in the final state, the technique for a single proton emission channel will be described here. This can be generalized quite easily to many nucleons in the final state.

Consider the case where a ^{28}Si projectile absorbs a virtual photon from the coulomb field of the target nucleus when passing through the target. The excited ^{28}Si which has an excess energy that corresponds to the energy of the virtual photon (ω), decays into ^{27}Al and a proton. The ^{27}Al could be in its ground state or any of the excited states (ϵ_i) which will decay by emitting one or more γ rays.

The invariant mass of the final state system can be written as

$$M_{inv} = M_o + \omega - \epsilon_i = M_1 + M_2 + \epsilon^* = \left|\overline{P}_1 + \overline{P}_2\right|$$

where M_o, M_1 and M_2 are the reset masses of the ^{28}Si, ^{27}Al and 1p respectively, and $\overline{P}_1$ and $\overline{P}_2$ are the 4 momentum vectors of the ^{27}Al and the 1p respectively. Thus, the excitation energy of the final state 1p+^{27}Al system is,

$$\epsilon^* = Q + \omega - \epsilon_i$$

where $Q = M_o - (M_1 + M_2)$ is the Q value of the reaction. For this system with two particles in the final state,

$$\left|\overline{P}_1 + \overline{P}_2\right|^2 = M_1^2 + M_2^2 + 2\sqrt{P_1^2 + M_1^2}\sqrt{P_2^2 + M_2^2} - 2P_1P_2\cos(\theta)$$

where θ is the angle between the two momentum vectors. By measuring the momentum P_1 and P_2 and the opening angle θ, one can calculate the invariant mass and hence the final state energy ϵ^*.

The implementation of the kinematics in the data analysis is done by performing a kinematically constrained fit, the construction of which follows the same outline discussed earlier. In this fit, it is assumed that the decaying Si nucleus has the same velocity as the beam track, but that the invariant mass is increased by the final state energy which is introduced as a variable in the fit. Two center of mass decay angles (θ^* and ϕ^*) are also introduced as variables, along with the horizontal and vertical slopes and intercepts of the incoming track. In this analysis, θ^* is defined as the polar angle of the ^{27}Al momentum vector with respect to the beam momentum vector in the rest frame of the projectile (because of our assumption that the velocity of the projectile is unchanged in the EMD process, this is also the rest frame of the excited state), and ϕ^* is the azimuthal angle of the decay plane about the beam momentum vector, referred to the horizontal plane. The masses of the final state particles were obtained from reference [61].

The kinematic fit imposes two additional constraints beyond those required by the geometric fit for the 1p+^{27}Al system since the total number of parameters needed to described the reaction kinematics is only 7. The additional constraints can be viewed as imposing conservation for the x and z components of momentum.

This fitting technique was found to be very useful in reconstructing the 1n+^{27}Si system in which the measurement of the momentum of the neutron is poor, but the position is accurately determined ($\approx$ 2cm). If the energy measurement is counted as a measurement (it carries very little weight due to its large error) in the fit, we obtain the same number of additional constraints for the kinematic fit of the 1n+^{27}Si system, as in the 1p+^{27}Al system.

2.3 Optimal Track Fitting

The optimal track fitting is a method which attempts to find the closest fit for a given set of points obtained under the change in the track direction due to multiple scattering along the path length. Conventional fitting operations that involve extracting track parameters usually neglect the effects due to multiple scattering or, degrade the errors in the measuring points to account for the scattering. Both of these procedures do not exploit the information from the detectors effectively.

The technique used in this analysis is the method described by Lutz [62], in which the "observed" value of the scattering angle is zero and the error in the observation is the calculated rms value of the scattering angle projected onto a plane. Since each parameter is accompanied by an observation, this method introduces no change in the number of degrees of freedom of the fit.

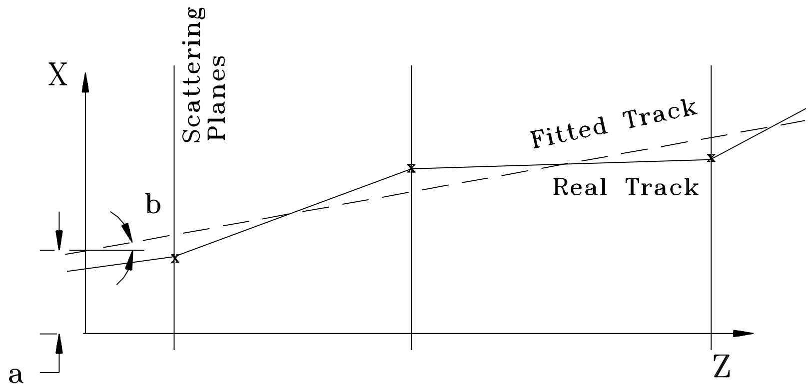

Figure 5.8: Effect of multiple scattering.

For simplicity, let us consider a region in two dimensions as shown in Figure 5.8. The multiple scattering along the trajectory can be replaced by a set of scattering planes which does not necessarily coincide with the measurement planes. The measured coordinates ξ_i can be fitted by a kinked trajectory whose position U_i in the measuring plane is parametrized by,

$$U_i = a + bz_i + \sum_J \alpha_J(z_i - z_J)\Theta_J$$

where a and b are the position and the slope of the incoming track, α_J is the kink in the scattering plane J and the parameter Θ_J is introduced to restrict scatters ahead of the measuring planes where

$$\Theta_J = \begin{cases} 1 & \text{for z} \geq 0 \\ 0 & \text{for z} < 0 \end{cases}$$

The χ^2 to be minimized in this situation by can be written as,

$$\chi^2 = \sum_i \frac{(\xi_i - U_i)^2}{\sigma_i^2} + \sum_J \frac{(\beta_J - \alpha_J)^2}{\sigma_J^2}$$

where σ_i is the rms measuring error of plane i and σ_J is the rms of the scattering angle β_J in the scattering plane J. It should be noted that knowing the value of β_J (in this case zero), compensates the additional parameters and thus keeps the number of degrees of freedom the same as that mentioned above.

In this analysis we introduce parameters to account for the multiple scattering in the horizontal plane for both the proton and the heavy ion tracks in the three regions where significant amounts of material are concentrated; namely the target, DC1 and DC2. It should be mentioned here that the energy loss resulting from the tracks passing through the target is also corrected.

3 Results

3.1 Efficiencies

Approximately 75% of the 1p events that were selected from the cross section analysis were reconstructed successfully. The major loss arises from demanding that there is exactly one hit in each counter of the beam vertex detector. Due to dead or noisy strips in the detector this criterion results in a loss of 15% of the events. By this, certain values of the beam angle and position are excluded. By failing to locate a sufficient number of hits in either DC2 or DC3 within the roads established in the pad sections of these chambers, 5% of the events are lost. (Due to the proximity of DC1 to the heavy ion track, there is a loss of the proton hit in 20% of the cases, but this does not affect the reconstruction of the event). Finally, due to either the geometric or kinematic fit failing to converge, 5% of the events are lost in the reconstruction stage. The remaining losses are quite small and it is obvious that they are not related to any particular event topology. The distributions of geometrical and kinematic quantities closely resemble those obtained in the simulation (described in the next section). Therefore it is assumed that any biases due to reconstruction inefficiencies are negligible.